Chapter – 4

Co-adsorption mechanism of organic pollutants on $NiFe_2O_4$/GO nanostructures: Experimental and molecular dynamics studies

4.1 Introduction

Several adsorbents have been developed for the removal of organic pollutants from wastewater. There have been reports of ciprofloxacin removal from water by adsorption on modified coal fly ash, molecularly imprinted polymers, clay materials, etc. [37,163,164]. Activated carbon, activated charcoal, and asphalt carbon have been widely used for the removal of different dyes from wastewater [165–167]. In this context, graphene oxides (GO) have attracted extensive attention in removing organic pollutants by adsorption due to their large surface area, different types of oxygen functional groups, and good dispersion in water[168–172]. Pollutant removal by adsorption requires adsorbent separation and recovery for each subsequent cycle. But, adsorbents, such as GO, having high aqueous dispersion, are difficult to isolate, increase the process cost, and can cause secondary pollution.

Separation and recycling of adsorbent particles is a major issue in removing pollutants. Magnetic separation of adsorbent particles is an efficient and economical solution for separating adsorbent nanoparticles easily. Superparamagnetic nano-adsorbents can be magnetized and de-magnetized by imposing or removing an external magnetic field. For this reason, magnetic ferrite nanoparticles have frequently been used for many adsorption applications[155]. Given this, $NiFe_2O_4$ nanoparticles are a practical choice because of their superparamagnetic properties and chemical stability[110,173–176]. For instance, Liu et al. developed the functionalized porous 3D-$NiFe_2O_4$ adsorbent for the simultaneous adsorption of fluoroquinolones and heavy metals from wastewater[110]. Darwish et al. reported $NiFe_2O_4$ nano-magnets for removing 2-nitrophenol[177]. Zeynep and co-workers fabricated $NiFe_2O_4$ for antimony removal from wastewater[175]. There are a few more reports on the use of $NiFe_2O_4$-based adsorbents for the removal of different organic pollutants[178,179].

The GO adsorbent can be recovered efficiently by magnetic decantation when combined with superparamagnetic $NiFe_2O_4$. Moreover, the $NiFe_2O_4$/GO composite would offer a larger variety of adsorption sites[180]. There are published articles in the literature on the adsorption properties of $NiFe_2O_4$/GO composite materials. For instance, Lingamdinne et al. used $NiFe_2O_4$/GO composite materials to remove hazardous materials such as metals and radionuclides from wastewater [180–182]. Large organic molecules like MG and CIP having two or more possible anchoring sites can interact with different available sites on an adsorbent. In other words, different types of sites in composite adsorbents can adsorb an adsorbate molecule through multiple links. But to date, there is no published report on the co-adsorption of two organic pollutants on a $NiFe_2O_4$/GO composite. Therefore, using a composite adsorbent is critical for a co-adsorption case. Hence, the present report investigates the simultaneous removal of MG and CIP on a $NiFe_2O_4$/GO composite from an aqueous medium.

Elucidating the molecular-level adsorption mechanism is critical to the co-adsorption problem. Adsorption isotherms have limited molecular-level insight for composite adsorbents with a variety of adsorption sites. Frequently, the same adsorption data fit multiple isotherms models quite closely, making any conclusion regarding the adsorption mechanism from such an investigation difficult. Keeping this in view, we conducted large-scale classical molecular dynamics (MD) simulations for a molecular-level comprehension of the problem. Classical MD simulations have previously been used to simulate molecular interactions, typically in problems with a single adsorbate [113,114]. Usually, the dispersion of a few solute molecules is considered in an aqueous medium to simulate a dilute solution scenario. Hence, the results also include solvent entropy effects. Few studies have used large-scale classical MD to gain molecular-level insight into a co-

adsorption problem, especially in conjunction with parallel experimental investigations[183–185].

Considering the above discussion, this chapter starts with the preparation of GO by the modified Hummer method. The $NiFe_2O_4$ nanoparticles were precipitated on GO flakes by a one-step hydrothermal method[186]. The obtained $NiFe_2O_4$/GO material was characterized by various characterization techniques such as TEM, XRD, XPS, FTIR, and BET (nitrogen adsorption-desorption isotherms) to confirm the structural aspects of the material. The co-adsorption properties of the composite nanoparticles towards CIP and MG in an aqueous solution were investigated. Classical MD simulations were simultaneously carried out to understand the molecular interactions involved in the co-adsorption through appropriate radial distribution function (RDF) analysis. Experimental and classical MD computational results were combined to better understand the mechanism of co-adsorption or competitive adsorption on $NiFe_2O_4$/GO nanocomposites.

4.2 Experimental section

The precursor compounds $Ni(NO_3)_2.6H_2O$ (Merck), $Fe(NO_3)_3.9H_2O$ (Merck), NaOH (Merck), graphite powder (Merck), $KMnO_4$ (Merck), H_2O_2 (Qualigens), H_2SO_4 (Merck), CIP (Merck), and MG (Merck) were utilized without any further purification. Other chemicals used were of AR grade. Double distilled water (DW) was used as a solvent in all the reactions.

4.2.1 GO synthesis

GO was synthesized by the modified Hummer method. First, 1.25g $NaNO_3$ and 2.50g graphite powder were mixed in 60 ml of concentrated H_2SO_4 in an ice bath. Then, 7g $KMnO_4$ was added pinch-wise to this mixture with continuous stirring at a temperature below 20°C. This reaction mixture was stirred for 4 hours at 35°C. Next, 115ml DW was

gradually added to this mixture and heated at 98°C for 15 min. The above solution was further diluted with 350 ml DW. The addition of 6ml H_2O_2 to the sample solution with vigorous stirring at 25°C several times until the washing liquid turned neutral. Then, the sample was dried in an oven at 60°C to obtain black flakes of GO.

4.2.2 Hydrothermal synthesis of the $NiFe_2O_4$/GO composite

The prepared $NiFe_2O_4$/GO composite had an equal weight percentage of $NiFe_2O_4$ and GO. First, an appropriate amount of finely crushed graphene oxide in 30ml DW was sonicated for an hour. On the other hand, 0.291 g of $Ni(NO_3)_2.6H_2O$ and 0.808 g of $Fe(NO_3)_3.9H_2O$ were mixed in 40 ml of distilled water and kept on a magnetic stirrer for one hour. The dispersed GO was added to the prepared salt mixture. Then, 1M NaOH was added dropwise to the above reaction mixture until the pH of the reaction mixture was 12. A brown precipitate was formed with the addition of NaOH. For better mixing, the reaction mixture was stirred for three more hours. This reaction mixture was transferred into an autoclave and heat treated at 180°C for 24 hours. Then, the sample obtained was carefully washed with distilled water and ethanol and dried in the oven at 80°C. Using the described procedure, nanocomposites of $NiFe_2O_4$ and GO were synthesized with varying $NiFe_2O_4$ weight percentages of 10%, 50%, and 75%, relative to the GO in the sample. Among these, the 10% $NiFe_2O_4$/GO composite exhibited poor magnetic properties, while the 75% $NiFe_2O_4$/GO composite showed limited adsorption capacity. Therefore, only the 50% $NiFe_2O_4$/GO composite was selected for further investigation of the co-adsorption of CIP and MG from aqueous solutions. This composite was hereafter referred to as $NiFe_2O_4$/GO throughout the thesis.

4.2.3 Adsorption studies

Several batch experiments were performed to quantify the adsorption capacity of $NiFe_2O_4$/GO for the co-adsorption of CIP and MG. Stock solutions of 100 ppm CIP and 45 ppm of MG were prepared in distilled water. These stock solutions were appropriately diluted before use in different adsorption experiments. Equal volumes of diluted (10 ml) CIP and (10 ml) MG solutions were mixed and used in all adsorption experiments. The optimum adsorbent amount was determined by conducting (24-hour adsorption) experiments with different amounts of $NiFe_2O_4$/GO adsorbent (20-70mg). Experiments were also performed at different pH conditions (attained by adding an appropriate amount of 0.1M NaOH or HCl). A fixed amount of adsorbent was added into the 20 ml mixture of 15 ppm CIP and 5 ppm MG solution at different pH and agitated for 24 hours. All adsorption experiments were carried out at room temperature (298.15 K).

Adsorption experiments were initially conducted on separate single-component aqueous solutions of CIP and MG. These are hereafter called single CIP component and single MG component systems. Adsorption experiments were also conducted on binary solutions of CIP and MG. For adsorption isotherm investigations, an optimum amount of $NiFe_2O_4$/GO was mixed into a 25 ml conical flask having different initial concentrations of CIP (9-36 ppm) and MG (3-12 ppm). These mixtures were agitated on a shaker for 24 hours (at a constant temperature) to find the equilibrium adsorption capacity (q_e). The adsorbent was separated by a magnet, and the concentrations of MG and CIP in the supernatant were determined by UV-visible spectroscopy. Note the volume of the adsorbate solution 20 ml for all adsorption experiments conducted in this research work.

Adsorption kinetics was investigated by adding an optimum amount of adsorbent into the conical flask with 20 ml of individual 15 ppm CIP and 5 ppm MG. Then, at regular time intervals, the adsorbent was separated by a magnet, and the concentrations of MG and CIP in the supernatant were determined, as earlier, by UV-visible spectroscopy.

4.2.4 Computational methodology

The Gaussview 6.0 software package was used for building the molecular models of GO, CIP, and MG (Figure 4.1). The structures of these molecules were optimized by the Modified Neglect of Diatomic Overlap (MNDO) (including d-orbitals) method. All the parameters of the water molecule were taken from the TIP3P water model (Table 4.1). A GO sheet of 194 atoms was constructed by Gauss view software. The structure of the GO sheet was optimized by DFT calculations on Gaussian 16 software. These calculations used a 6-311G++(d,p) basis set for all atoms in GO and the B3LYP (Becke-3-Parameter-Lee-Yang-Parr) functional. Next, the optimized GO sheet was placed in the middle of a parallelopiped simulation box (dimension; 28 Å x 16 Å x 50 Å) such that the GO sheet was perpendicular to the z-axis of the box. The simulation box was modelled by Scienomics released software Materials and Process Simulation (MAPS) version 4.1.1 [143].

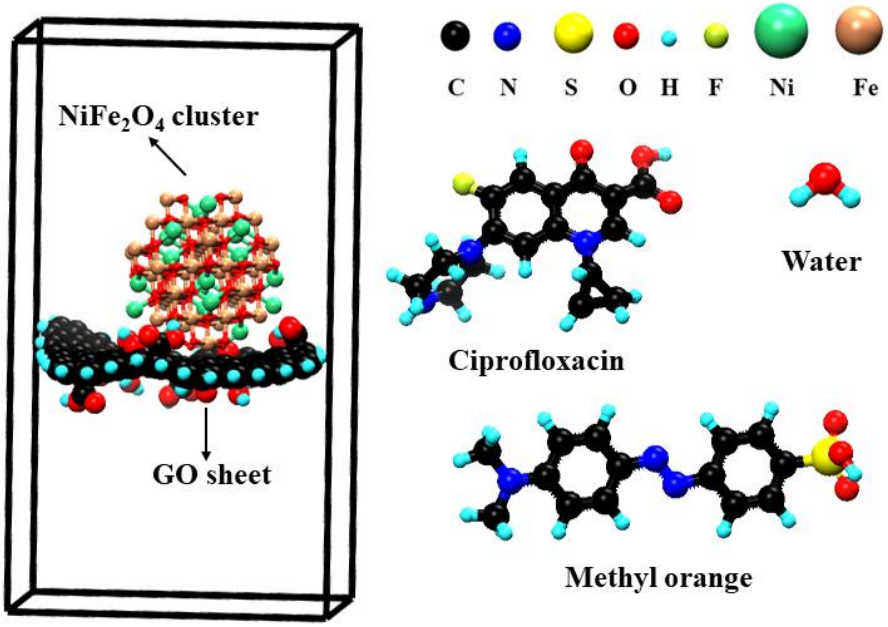

Figure 4.1 The initial simulation box showing the $NiFe_2O_4$ cluster placed adjacent to the GO sheet.

Table 4.1 TIP3P water model parameters.

Parameter	Value
O_W-H_W bond (k_b , r_0)	450 Kcal/mol/Å^2, 0.9572 Å
H_W-O_W-H_W (k_a , θ)	55 Kcal/mol, 104.52˚
O_W charge	-0.834
H_W charge	0.417

The nickel ferrite unit cell (MP-22684) structure (from the material project interface [187] was multiplied to construct its 3 x 3 x 3 supercell. Then, a nickel ferrite cluster having 139 atoms, was cleaved from this supercell using the MAPS software. The $NiFe_2O_4$ cluster was placed adjacent to the GO sheet at ~2 Å distance in the simulation box (Figure 4.1). This model of the adsorbent is abbreviated as MNFGO in the rest of the manuscript. Next, 2 CIP, 2 MG, and 500 TIP3P water molecules were filled in the space on each side of the GO sheet in the simulation box using the Amorphous Builder tool of the MAPS software. Figure 4.2 displays the initial configuration of the simulated model system.

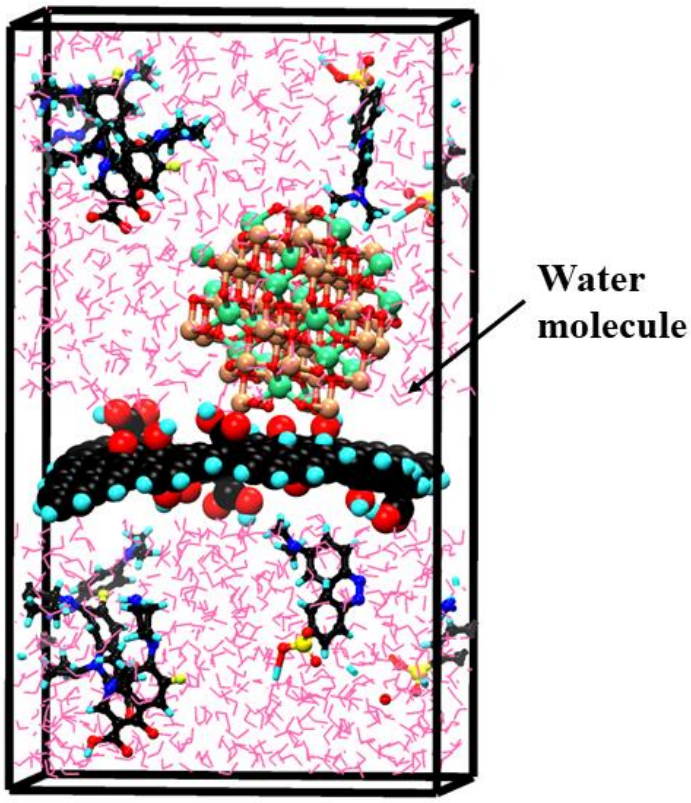

Figure 4.2 Initial configuration of simulation box after filling CIP, MG, and water molecules on both sides of the MNFGO surface.

Classical MD simulations were carried out on the LAMMPS (Large-scale Atomic/Molecular Massively Parallel Simulator) software. A modified 'Drieding' force field was utilized for the molecular dynamics simulations[134]. The Lennard-Jones (LJ) 12-6 potential equation defines the potential energy contribution by the non-bonded interaction part of the Dreiding force field (Equation 4.1)[134];

$$E_{lj}^{LJ} = 4\varepsilon_0 \left[\left(\frac{\sigma_0}{r_{ij}} \right)^{12} - \left(\frac{\sigma_0}{r_{ij}} \right)^{6} \right] \quad (4.1)$$

In Eq. (4.1), $\varepsilon_0$is the potential well depth, $\sigma_0$denotes the van der Waal's radii, $r_{ij}$is the interatomic distance between atom types *i* and *j*. Table 4.2 presents the LJ 12-6 parameters for all atom types used in this study. The temperature of the simulation box was fixed at

298.15 K using a Nose-Hoover thermostat. Periodic boundary conditions were applied on all three dimensions of the simulation box. The Particle Mesh method calculated the Coulombic interactions between atoms with the real space cut-off distance fixed at 12 Å**.** For equilibration of the volume of the simulation box, the model was subjected to an NPT ensemble MD run of ten nanoseconds (ns) with 0.5 femtoseconds (fs) time-step. The GO sheet was kept fixed (or rigid) during the MD simulation runs.

Table 4.2 Lennard-Jones (LJ) 12-6 potential parameters for different atom types of adsorbent ($NiFe_2O_4$ and GO part), adsorbates (CIP and MG), and solvent (H_2O) for non-bonded interaction.

Atom type	**ε_0(Kcal/mol)**	**σ_0(Å)**
Ni ($NiFe_2O_4$)	0.0150	2.834
Fe ($NiFe_2O_4$)	0.0550	4.540
O_3 (lattice oxygen of $NiFe_2O_4$)	0.0957	3.4046
C_2 (ring carbon of CIP, GO, and MG)	0.0951	3.8983
C_3 (ring carbon of CIP, GO, and MG)	0.0951	3.8983
C_R (ring carbon of CIP, GO, and MG)	0.0951	3.8983
H_ (hydrogen attached to the ring carbon of CIP, GO, and MG)	0.0152	3.1950
H__B (carboxylic hydrogen of GO)	0.0001	3.1950
H_W (water)	0.0000	0.0000
H_S (sulfonic hydrogen of MG)	0.0152	3.1950
H_C (carboxylic hydrogen of CIP)	0.0152	3.1950
N_3 (amino nitrogen of MG)	0.0774	3.6621
N_R (azo nitrogen of MG)	0.0774	3.6621

O_A (carbonyl oxygen of GO)	0.0957	3.4046
O_S (sulfonic oxygen of MG)	0.0957	3.4046
O_2 (epoxide oxygen of GO)	0.0957	3.4046
O_M (Carboxylic oxygen of CIP)	0.0957	3.4046
O_C (carbonyl oxygen of CIP)	0.0957	3.4046
O_R (alcohol oxygen of GO)	0.0957	3.4046
O_W(water)	0.1020	3.1880
S_3 (sulfonic sulfur of MG)	0.3440	4.0300
F_ (Fluoride group of CIP)	0.0725	3.472

4.3 Results and discussion

4.3.1 Material characterizations

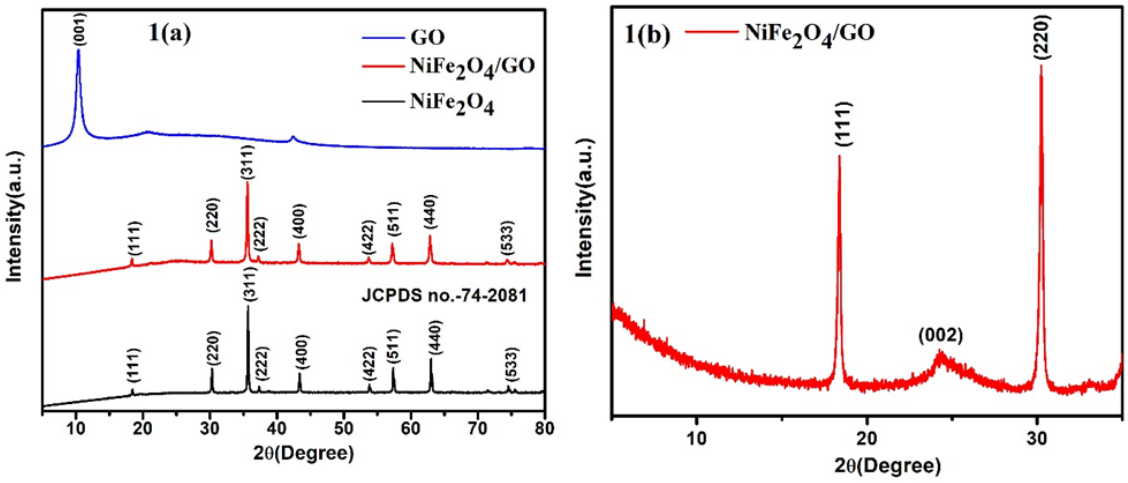

Figure 4.3 (a)XRD patterns of the prepared GO, $NiFe_2O_4$/GO, and $NiFe_2O_4$ samples, (b) HR-XRD of $NiFe_2O_4$/GO.

Figure 4.3a shows the XRD patterns of pure $NiFe_2O_4$, GO, and $NiFe_2O_4$/GO composite. It displays the XRD plot for the GO sample. The intense XRD peak at 10.3° is characteristic

of the (001) reflection of GO[188]. In the XRD pattern of pure $NiFe_2O_4$, diffraction peaks are observed at 18.4°, 30.2°, 35.7°, 37.3°, 43.3°, 53.8°, 57.2°, 62.9° and 74.4° (2θ) conforming to (111), (220), (311), (222), (400), (422), (511), (440), and (533) planes of inverse spinel $NiFe_2O_4$ structure as per JCPDS File 74-2081[189]. No peaks, other than those of $NiFe_2O_4$, were observed in the XRD. In the case of the $NiFe_2O_4$/GO composite, all the diffraction peaks match that of $NiFe_2O_4$ (JCPDS File 74-2081). The GO peak in the $NiFe_2O_4$/GO pattern is not visible due to the high intensity of the diffraction peaks of $NiFe_2O_4$. Figure 4.3b shows the HR-XRD of $NiFe_2O_4$/GO sample from 5° to 40° 2θ range. The peak at 24.3° represents the (002) plane of GO. There is no peak in the 10° to 15° 2θ regions of these XRD patterns, indicating that GO sample got reduced to r-GO (reduced-GO) on precipitation of $NiFe_2O_4$ nanoparticles on the GO sheets.

The magnetic property of the adsorbent facilitates its separation from the aqueous (wastewater) medium economically. Figure 4.4a shows the plot between magnetization M_s and the applied magnetic field for $NiFe_2O_4$ and $NiFe_2O_4$/GO samples. The saturation magnetizations of $NiFe_2O_4$ and $NiFe_2O_4$/GO samples were 38.71 and 10.42 emu g^{-1}, respectively. The reduction in magnetic properties of the $NiFe_2O_4$/GO composite was due to the presence of the non-magnetic GO sheets in the composite. Despite that, the M_s of the composite is sufficient for separating its particles from the solution by a magnet.

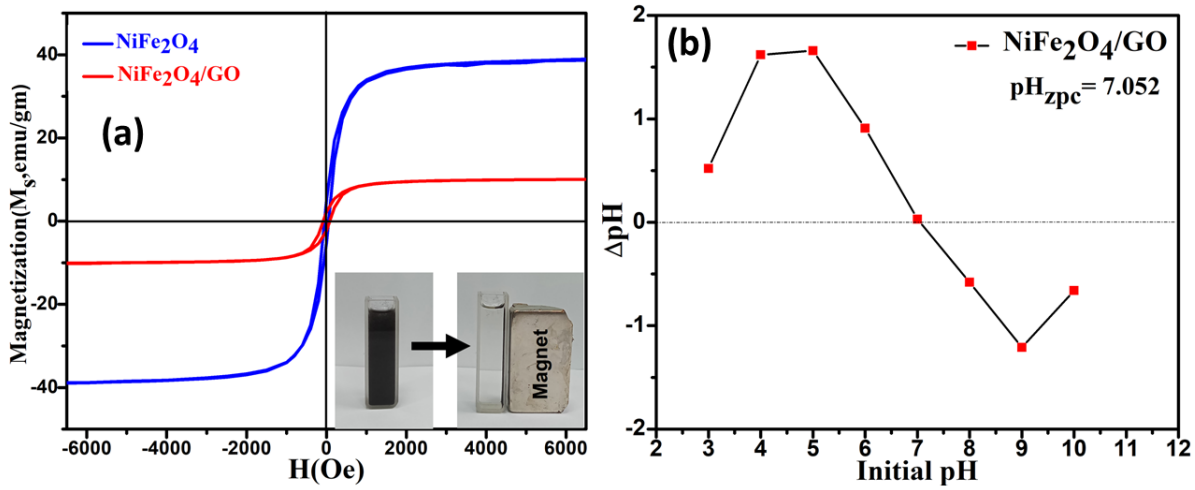

Figure 4.4 (a)VSM curves of $NiFe_2O_4$ and $NiFe_2O_4$/GO particles, and (b) Graph for pH_{zpc} of $NiFe_2O_4$/GO composite.

Zero-point charge (pH_{zpc}) is the pH at which the total surface charge density of the adsorbent is zero. The section 2.2.1.11 of previous chapter 2 details the experiments conducted to find the pHzpc for the $NiFe_2O_4$/GO composite. At pH < pH_{zpc}, adsorbent possesses a positively charged surface, while at pH > pH_{zpc}, adsorbent possesses a negatively charged surface. The change in the adsorbent's surface charge affects the adsorbent's adsorption capacity for the same adsorbates. In this work, the pH_{zpc} of $NiFe_2O_4$/GO is observed at 7.02, almost at the neutral pH (Figure 4.4b).

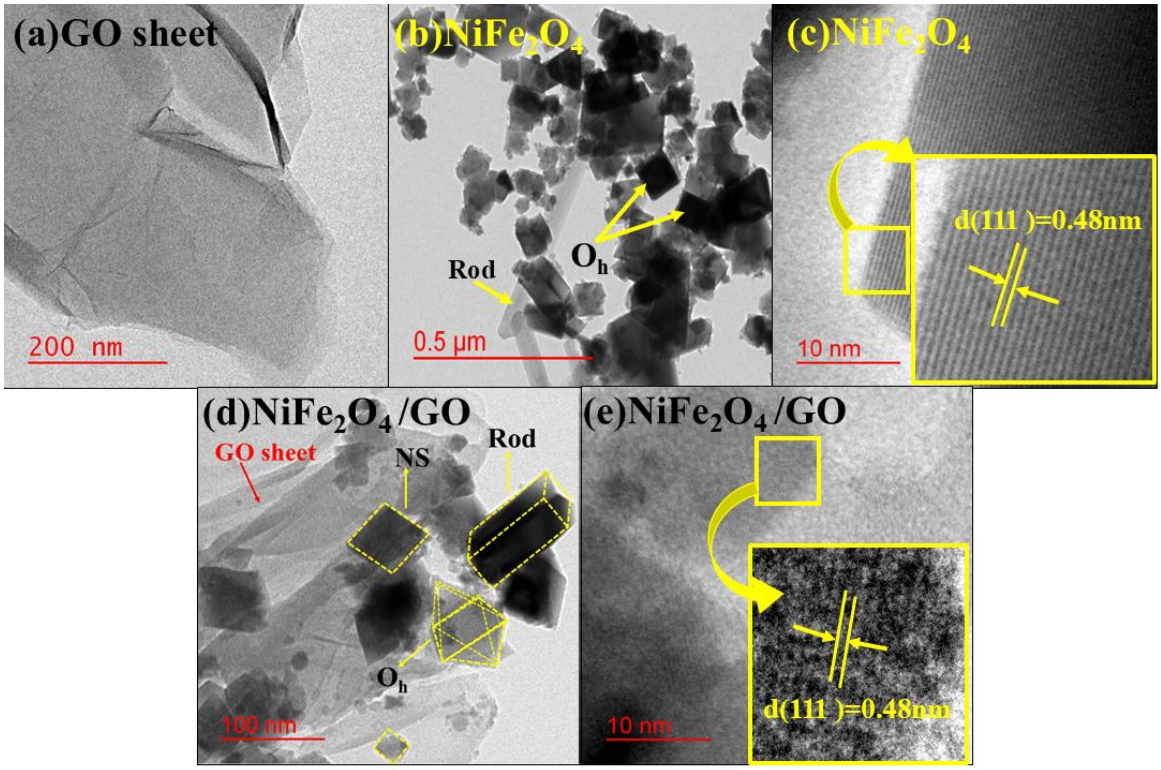

Figure 4.5 (a) TEM image of GO, (b, and c) TEM and HR-TEM images of the $NiFe_2O_4$, (d, and (e) TEM and HR-TEM images of $NiFe_2O_4$/GO composite. Here, NS denotes nanosheet, and O_h stands for octahedral.

Figure 4.5a shows wrinkled pure GO sheets. Figure 4.5b shows the morphology of pure $NiFe_2O_4$ which represents the octahedron and nanorod shape of $NiFe_2O_4$. The ImageJ software was used to analyze the TEM images of the pure $NiFe_2O_4$ and $NiFe_2O_4$/GO composite sample. The interplanar distance (d) of fringes shown in HR-TEM of pure $NiFe_2O_4$ was 0.48 Å attributed to the (111) $NiFe_2O_4$ crystal plane. Figure 4.5d and 4.5e show different TEM images of the prepared $NiFe_2O_4$/GO composite. Figure 4.5d shows that the $NiFe_2O_4$/GO sample contains rod, octahedron-shaped, and 2D nanosheets of $NiFe_2O_4$ nanostructures dispersed over wrinkled GO sheets. Figure 4.5e displays an HR-TEM image of the same sample. The indicated fringe's interplanar distance (d) in this image was also 0.48 Å, corresponding to the (111) $NiFe_2O_4$ crystal plane. It confirms the loading of $NiFe_2O_4$ on the GO sheets.

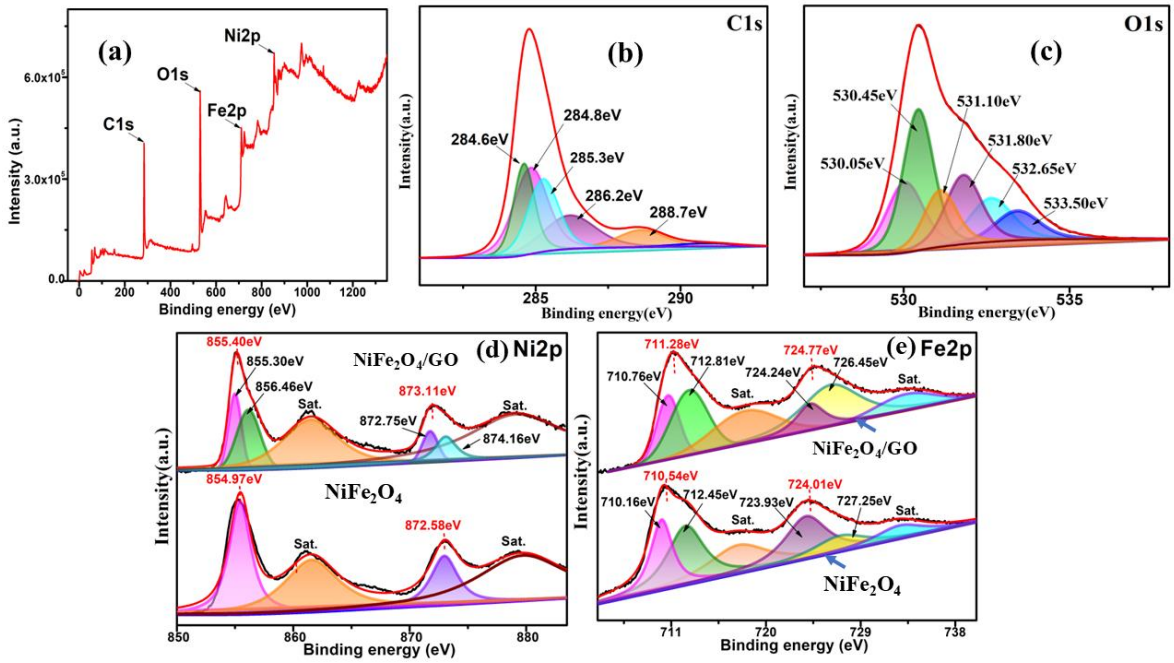

Figure 4.6 The XPS survey spectrum of $NiFe_2O_4$/GO composite, XPS deconvoluted spectra of (b) C1s of $NiFe_2O_4$/GO, (c) O1s of $NiFe_2O_4$/GO, (d) Ni2p, and (e) Fe2p of both pure $NiFe_2O_4$ and $NiFe_2O_4$/GO composite.

The X-ray photoelectron spectroscopy (XPS) technique has been used to determine the chemical species on the surface of $NiFe_2O_4$/GO composite particles. The survey XPS spectrum of the composite sample contains Ni, Fe, O, and C elements without other impurities (Figure 4.6a). In Figure 4.6b, C1s spectrum of $NiFe_2O_4$/GO composite is deconvoluted into 284.6eV, 284.8eV, 285.3eV, 286.2eV and 288.7eV corresponding to sp^2 carbon, sp^3 carbon, C-OH, C-O-C and O-C=O respectively[190,191]. Figure 4.6c shows the composite high-resolution O1s spectrum deconvoluted into six characteristic peaks at binding energies 530.05, 530.45, 531.1, 531.8, 532.65, and 533.5eV. The peak at 530.05eV is due to the lattice oxygen (M-O bond) in $NiFe_2O_4$[192]. Four other deconvoluted peaks in the O1s spectrum are for the oxygens in quinone O (530.45 eV), oxygen vacancy (531.1 eV), O=C–OH (531.8 eV), and C–O (epoxy and alkoxy) (532.65 eV)[193,194]. The peak at 533.5 eV could be due to oxygens in C–OH or physically or chemically adsorbed water[193].

Figure 4.6d shows the deconvoluted Ni2p spectrum. The $Ni2p_{3/2}$ and $Ni2p_{1/2}$ peaks appear at 855.40eV and 873.11eV binding energies, respectively. Moreover, the deconvolution of the $Ni2p_{3/2}$ peak reveals two peaks at 855.30eV and 856.46eV. These are typical of Ni^{2+} occupying tetrahedral and octahedral voids of the prepared sample [195]. The $Ni2p_{1/2}$ peak at 873.11eV also deconvolutes into two Ni2p spectrum peaks at 872.75 and 874.16eV. These correspond to Ni^{2+} ions in tetrahedral and octahedral voids. The peaks at binding energy 880.48 eV and 860.08 eV are satellite peaks (denoted as Sat.). Figure.4.6e deconvolutes the $Fe2p_{3/2}$ spectrum into peaks at 710.76eV and 712.81eV. The latter is characteristic of Fe^{3+} occupying octahedral and tetrahedral voids, respectively. The $Fe2p_{1/2}$ spectrum (725.03eV) deconvolutes into two peaks at 724.24eV and 726.45eV. These again represent Fe^{3+} occupying both octahedral and tetrahedral voids in the $NiFe_2O_4$ system. Besides this, the Fe2p spectrum also displays two satellite peaks at 718.48 eV and 733.63 eV (denoted as Sat.). The difference of binding energy of $Fe2p_{3/2}$ main peak and $Fe2p_{3/2}$ satellite peak is ~8.0 eV[196]. Satellite peaks and their distance from the Fe2p peak enables the classification and assignment of the HR-XPS deconvoluted peaks in the Fe2p region. Lima et al have shown that the presence of satellite peaks at a specified distance range from the Fe2p peak indicates only Fe^{3+} is present in the $NiFe_2O_4$ sample [196,197] Ni^{2+} and Fe^{3+} show double occupancy characteristics in the $NiFe_2O_4$/GO composite [195]. Thus, the $NiFe_2O_4$ component of the $NiFe_2O_4$/GO composite has neither an inverse nor direct spinel structure. In contrast, the pure $NiFe_2O_4$ nanoparticles prepared by an analogous hydrothermal technique have an inverse spinel structure. Another crucial observation is that XPS peaks of Ni2p and Fe2p shifted to higher binding energies after forming the $NiFe_2O_4$/GO composite compared to their positions in pure $NiFe_2O_4$ (Figure 4.6). This binding energy shifting points to the successful preparation of the composite sample.

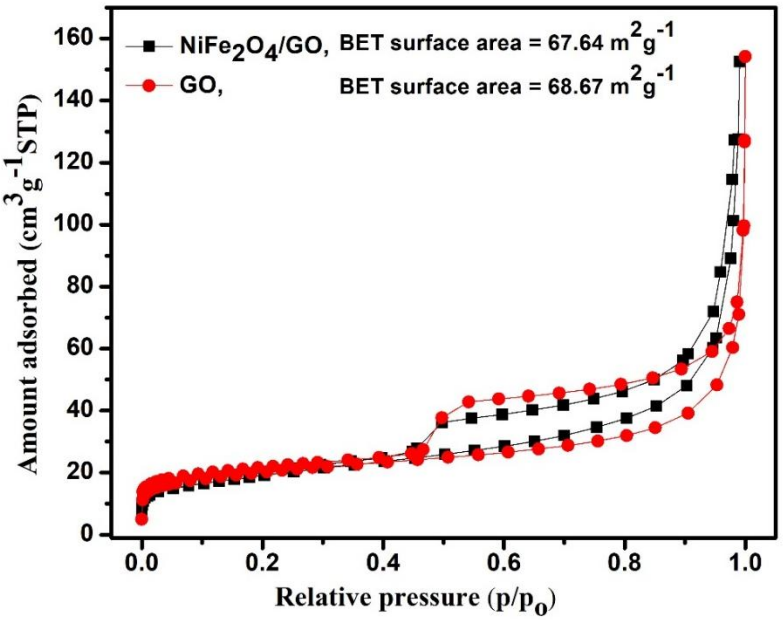

Figure 4.7 BET (Brunauer, Emmett, and Teller) curve of the pure GO and $NiFe_2O_4$/GO composite sample.

The adsorption capacity of an adsorbent also depends on its surface area. The BET N_2 adsorption-desorption isotherm was used to determine the surface area of the $NiFe_2O_4$/GO composite (Figure 4.7). The observed plot is a type IV isotherm, and the loop in the graph indicates that the GO and $NiFe_2O_4$/GO composite particulates are mesoporous [198]. The BET surface area of GO was 68.67 m^2g^{-1}. After composite formation, the BET surface area of the $NiFe_2O_4$/GO composite decreased to 67.64 m^2g^{-1}. Therefore, this reduction does not reflect any significant structural change. Instead, it suggests that $NiFe_2O_4$ nanoparticles are uniformly dispersed on the GO sheets without substantial blocking of pores or collapse of the layered framework.

4.3.2 Adsorption studies

Figure 4.8a shows the effect of adsorbent dosage on the adsorption process. Control adsorption experiments were carried out at different $NiFe_2O_4$/GO adsorbent dosages between 0.020 to 0.070 g. The last (0.070 of $NiFe_2O_4$/GO) dosage displayed the best

adsorbent performance under a given set of conditions. The increase in % removal is due to an increase in the number of active sites with the amount of adsorbent dose. But increasing the adsorbent amount in the reaction mixture beyond a certain limit causes aggregation of adsorbent nanoparticles. The latter results in a lower specific adsorbent surface area. In the present case, the best CIP and MG removal by adsorption (over 24 hours) was demonstrated when the adsorbent amount was 0.070 g. Thus, 0.070 g of the adsorbent amount was used in all adsorption experiments reported in this Chapter.

Figure 4.8b shows the effect of the pH of the adsorbate solution on the adsorption of CIP and MG on the $NiFe_2O_4$/GO adsorbent. The solution pH was varied from 3.0-9.0. The pH of the adsorbate solution does not affect the adsorption of CIP on the $NiFe_2O_4$/GO nanoparticles. Contrary to this, the $NiFe_2O_4$/GO adsorbent particles demonstrated the best MG adsorption under neutral pH conditions. Acidic and basic adsorbate aqueous solutions demonstrated lesser MG removal capacity. Given that the pH_{zpc} of $NiFe_2O_4$/GO was 7.02, at pH<7.02, the adsorbent has a positive surface charge, while at pH>7.02, the adsorbent has a negative surface charge. It means that $NiFe_2O_4$/GO and MG molecules are positively charged at acidic pH, and at higher basic pH, both are negatively charged. Because of the same charge, electrostatic repulsion can be engendered between $NiFe_2O_4$/GO and MG molecules[39,199]. Overall, the best CIP and MG adsorption results were observed at neutral pH. Therefore, all adsorption studies were done at neutral pH with a 0.070 g adsorbent dose.

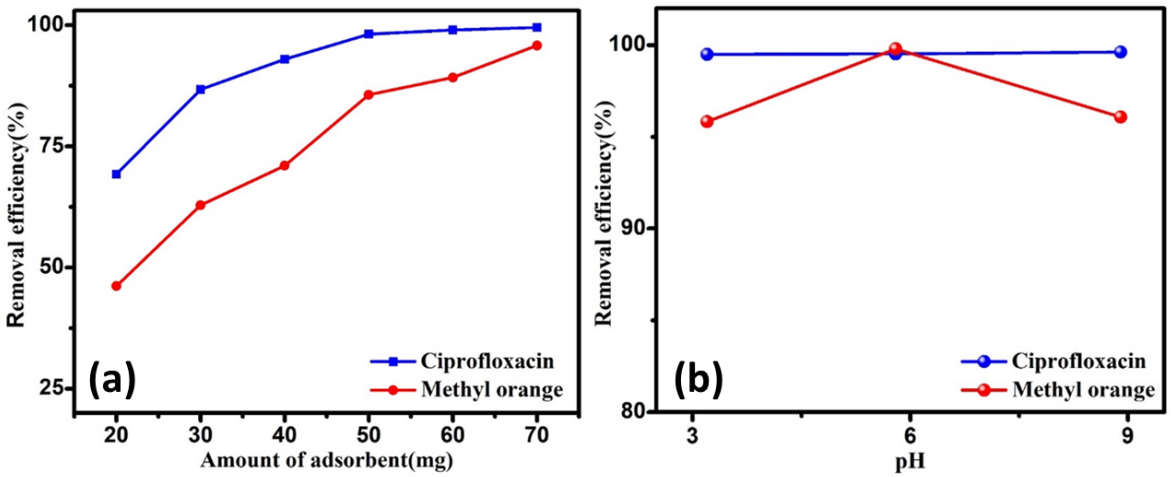

Figure 4.8 (a) Effect of amount of adsorbent ($NiFe_2O_4$/GO) on the co-adsorption of CIP and MG. (b) Effect of pH on the co-adsorption of CIP and MG. (Conditions- The binary solution of CIP and MG has equal volumes of 15 mg L^{-1} CIP and 5 mg L^{-1} MG solutions. All optimization experiments were done with 20ml of the adsorbate solution, and 300K temperature.)

Figures 4.9a and 4.9b show graphs plotted between the adsorption capacity (mg/g) of adsorbent ($NiFe_2O_4$/GO) versus time (in minutes) for single adsorbate systems. The adsorption capacity increased sharply in the initial 10 min in all cases due to the availability of the maximum number of active sites of $NiFe_2O_4$/GO adsorbent. Figure 4.9a shows that the adsorption capacity of CIP almost reached its q_e value by the end of the first hour. Figure 4.9b displays the change in the adsorption capacity of MG with time. The adsorption kinetics of MG is slower than CIP, and it can be concluded that the adsorbent ($NiFe_2O_4$/GO) has a higher affinity for CIP.

Pseudo-first-order and pseudo-second-order kinetics equations were applied to calculate the kinetics parameters of the adsorption of CIP and MG on the surface of $NiFe_2O_4$/GO [200]. The pseudo-first and second-order non-linear kinetics equations are provided in chapter 1 of this thesis.

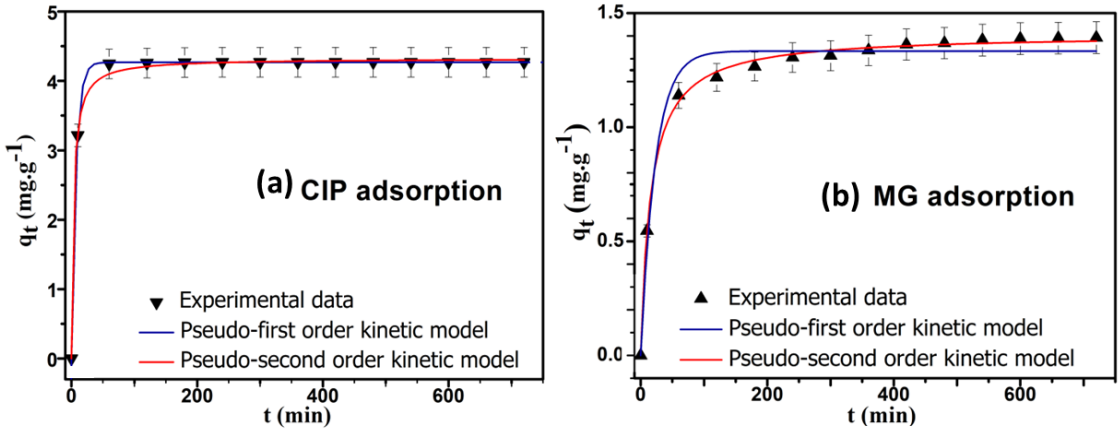

Figure 4.9 Adsorption kinetics for (a) CIP and (b) MG from their aqueous solutions. The concentration of aqueous solution of CIP only was 15 mg L^{-1}. The concentration of the aqueous solution of MG was 5 mg L^{-1}. All adsorption kinetics experiments were done with 20ml of the adsorbate solution, 0.070 g adsorbent dose, at neutral pH, and 300K temperature.

Table 4.3 Plots of adsorption capacity (mg/g) versus time for adsorption CIP and MG from their aqueous solutions.

Adsorbate	Pseudo-first-order kinetics			Pseudo-second-order kinetics		
	k_1(min^{-1})	q_e (mg.g^{-1})	R^2	k_2 (g.mg^{-1}.min^{-1})	q_e (mg.g^{-1})	R^2
CIP	0.1280	4.265	0.999	0.0578	4.343	0.981
MG	0.0523	1.310	0.976	0.0454	1.403	0.998

Table 4.3 shows the calculated kinetics parameters for single (CIP and MG) adsorbate systems. The CIP adsorption kinetics data fits the pseudo-first-order model better than the pseudo-second-order model. Pseudo-first-order kinetics points to a physical adsorption type adsorbent-adsorbate interaction. But the difference between the correlation coefficients (R^2) of the pseudo-first order and the pseudo-second-order fit is insignificant. The pseudo-second-order kinetics model fits better the MG adsorption data. Such

adsorption kinetics is indicative of chemisorption. In this case, the difference between the correlation coefficients of the pseudo-first-order and pseudo-second-order fit is significant.

The adsorption isotherms are plots between the equilibrium adsorption capacity (q_e) and the adsorbate's equilibrium concentration (C_e) in the solution at a constant temperature. Standard Langmuir, Freundlich, and Langmuir-Freundlich (LF) isotherm models cannot be used for multi-adsorbate systems. Hence, the multi-component extended versions of these equations were used to fit the co-adsorption isotherm data. Equations 4.2 to 4.7 represent expressions for the Extended Langmuir (EL) isotherm, Extended Freundlich (EF) isotherm and Extended LF (ELF) isotherm, respectively[201,202]Here subscript '*i*' is 1 for CIP and 2 for MG.

EL adsorption isotherm equations:

$$q_{e1} = \frac{(q_{m1} b_1 C_{e1})}{(1+b_1 C_{e1}+b_2 C_{e2})} \quad (4.2)$$

$$q_{e2} = \frac{(q_{m2} b_2 C_{e2})}{(1+b_1 C_{e1}+b_2 C_{e2})} \quad (4.3)$$

In Eq. (4.2) and (4.2), q_{m1} and q_{m2} represent the maximum monolayer adsorption capacities ($mg.g^{-1}$); b_1 and b_2 indicate Langmuir constants for CIP and MG, respectively ($L.mg^{-1}$).

EF adsorption isotherm equations:

$$q_{e1} = \frac{k_1 C_{e1}^{((1/n_1)+x_1)}}{(C_{e1}^{x_1}+y_1 C_{e2}^{z_1})} \quad (4.4)$$

$$q_{e2} = \frac{k_2 C_{e2}^{((1/n_2)+x_2)}}{(C_{e2}^{x_2}+y_2 C_{e1}^{z_2})} \quad (4.5)$$

In Eq. (4.4) and (4.5), k_1 and k_2 represent the Freundlich constants related to the affinity of the binding sites (L.mg^{-1}); n_1 and n_2 indicate constant representing adsorption intensity (where, n_1, n_2 >1); x_1, y_1, z_1 and x_2, y_2, z_2 denote binary correction coefficients.

ELF adsorption isotherm equations:

$$q_{e1} = \frac{(q_{m1} b_1 C_{e1}^{1/n_1})}{(1+b_1 C_{e1}^{1/n_1}+b_2 C_{e2}^{1/n_2})} \quad (4.6)$$

$$q_{e2} = \frac{(q_{m2} b_2 C_{e2}^{1/n_2})}{(1+b_1 C_{e1}^{1/n_1}+b_2 C_{e2}^{1/n_2})} \quad (4.7)$$

In Eq. (4.6) and (4.7), q_{m1} and q_{m2} represent the maximum monolayer adsorption capacities (mg. g^{-1}); n_1 and n_2 indicate constant representing adsorption intensity (where, n_1, n_2 >1); b_1 and b_2 represent LF affinity constants (L.mg^{-1}).

Table 4.4 Different Adsorption isotherm parameters for CIP and MG in binary system.

Adsorbate in binary system	**Extended Langmuir isotherm parameters**				
	q_{m1} **(mg.g^{-1})**	q_{m2} **(mg.g^{-1})**	b_1 **(L.mg^{-1})**	b_2 **(L.mg^{-1})**	**R^2**
CIP (CIP+MG)	13.570	---	0.945	---	0.771
MG (CIP+MG)	---	2.783	---	2.564	0.838
Adsorbate in binary system	**Extended Freundlich isotherm parameters**					
	x_i	y_i	z_i	k_i **(L.mg^{-1})**	n_i	**R^2**
CIP (CIP+MG)	0.417	1.770	4.826	18.205	3.60	0.997
MG (CIP+MG)	4.561	0.010	5.144	2.044	20.1	0.972
	Extended LF isotherm parameters					

Adsorbate in binary system	q_{m1} (mg.g^{-1})	q_{m2} (mg.g^{-1})	b_1 (L.mg^{-1})	b_2 (L.mg^{-1})	n_1	n_2	R^2
CIP (CIP+MG)	8.61	---	15.701	---	1.866	---	0.781
MG (CIP+MG)	---	2.50	---	24.505	---	1.933	0.750

The EL, EF, and ELF binary system equations were fitted to q_{ei} versus C_{ei} plots at ~300 K. Table 4.4 gives various binary system fitting parameters of the EL, ELF and EF isotherms to the q_{ei} versus C_{ei} plots. The correlation coefficients (R^2) values for EL and ELF equation fits to the q_{ei} versus C_{ei} plots range from 0.75 to 0.84. Hence, the R^2 values for the EL and ELF fits to q_{ei} versus C_{ei} plots are quite poor. In contrast, the fitting of the EF isotherm to the q_{ei} versus C_{ei} plots are much better. The R^2 for these fits range from 0.97 to 0.99. Hence, we conclude that the EF isotherm best fits the q_{ei} versus C_{ei} plots for CIP and MG. Figures 4.10a and 4.10b show the equilibrium EF isotherm equation fitting of the CIP and MG adsorption data. An EF isotherm fit indicates an adsorbent with heterogeneous adsorption sites. The latter agrees with the fact that $NiFe_2O_4$/GO adsorbent is a composite with different types of adsorption sites.

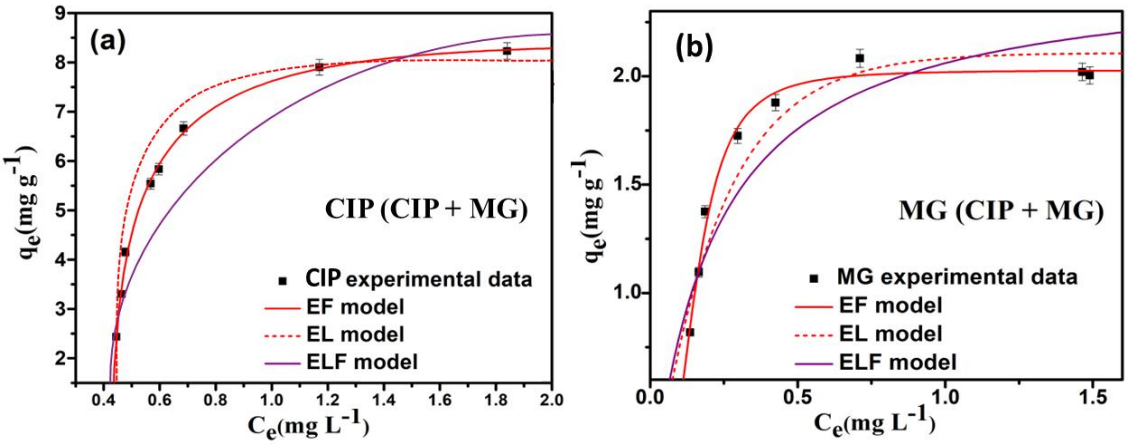

Figure 4.10 Extended adsorption isotherms for both (a) CIP and (b) MG adsorbates in a binary system. The binary solution is mixture of equal volumes of CIP and MG.

(Conditions- The concentration of CIP varies from 9 to 36 mg L^{-1} and MG from 3 to 12 mg L^{-1}. All adsorption isotherm experiments were done with 20ml of the adsorbate solution, 0.070 g adsorbent dose, for 24 hours adsorption time, at neutral pH, and 300K temperature.)

Figure 4.11 displays the FTIR spectra of pure $NiFe_2O_4$/GO and that of the $NiFe_2O_4$/GO sample after MG and CIP adsorption. A shift in FTIR peak position usually implies a change in the molecular bond's hybridization state or electron distribution[203]. The FTIR of the $NiFe_2O_4$/GO sample (Figure 4.11a) displays peaks at 408 and 597 cm^{-1}. These correspond to Ni-O and Fe-O stretching vibrations, respectively. The $NiFe_2O_4$/GO transmission spectra also consist of peaks of several oxygen-containing functional groups. These include the C-CO (891 cm^{-1}) stretching, C-O stretching band (1066 cm^{-1}), C-O-C (1212.5 cm^{-1}), unoxidized aromatic C=C bond vibrations (1562 cm^{-1}), stretching vibration of C=O (1728 cm^{-1}) and a broad peak of O-H vibration around at 3424.3 cm^{-1}.

After the adsorption of CIP and MG (Figure 4.11b), characteristic C-CO, C-O-C, C-O, and C=O stretching vibration peaks shift to higher wavenumbers, indicating CIP and MG interact with the $NiFe_2O_4$/GO surface through these functional groups. The new peak at 1450 cm^{-1} represents both S-O and C-F stretching vibrational peaks. It is evidence for MG adsorption to $NiFe_2O_4$/GO through the SO_3^- group and the interaction between CIP and $NiFe_2O_4$/GO.

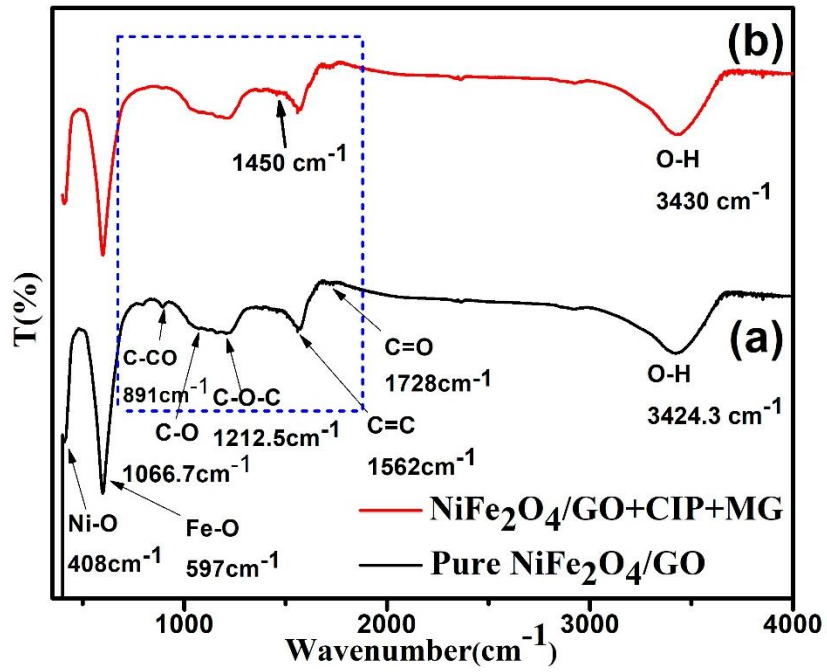

Figure 4.11 FTIR spectra of (a) pure $NiFe_2O_4$/GO, (b) CIP and MG adsorbed $NiFe_2O_4$/GO.

Recyclability tests were performed on the $NiFe_2O_4$/GO sample to evaluate its stability for repeated adsorbent use (Figure 4.12a). After each adsorption cycle, the adsorbent ($NiFe_2O_4$/GO) was regenerated by washing it several times with double distilled water followed by ethanol. Then, the washed $NiFe_2O_4$/GO was kept in the oven and dried for the next adsorption cycle. Four adsorption cycles were performed with the same $NiFe_2O_4$/GO sample using this procedure. The adsorption capacity decreased to 96% of the first adsorption cycle for the adsorption of CIP. Figure 4.12b displays the XRD of the $NiFe_2O_4$/GO sample after its reuse for the fourth cycle. All peaks observed in a fresh $NiFe_2O_4$/GO sample were also observed in the XRD of the reused sample. Thus, the $NiFe_2O_4$/GO sample was quite stable even after the 4th adsorption cycle (Figure 4.12b).

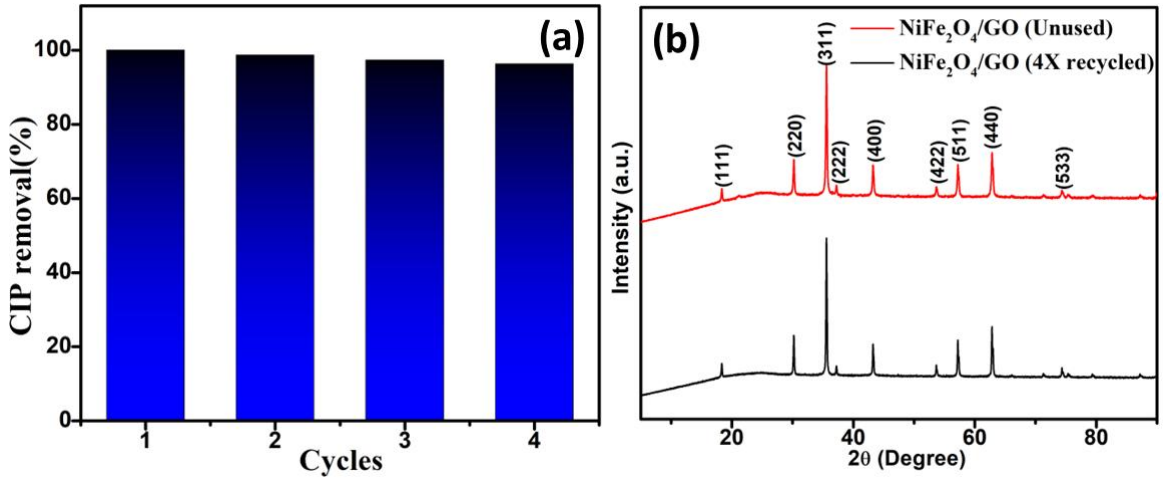

Figure 4.12 (a) Recyclability graph of $NiFe_2O_4$/GO adsorbent up to 4 cycles, (b) XRD graph of the recycled $NiFe_2O_4$/GO sample. The binary solution of CIP and MG was prepared by mixing equal volumes of 15 mg L^{-1} CIP and 5 mg L^{-1} MG solutions. The adsorbent recyclability experiments were done with 20 ml of the adsorbate solution, 0.070 g adsorbent dose, at neutral pH, and 300K temperature.

4.3.3 MD simulations results

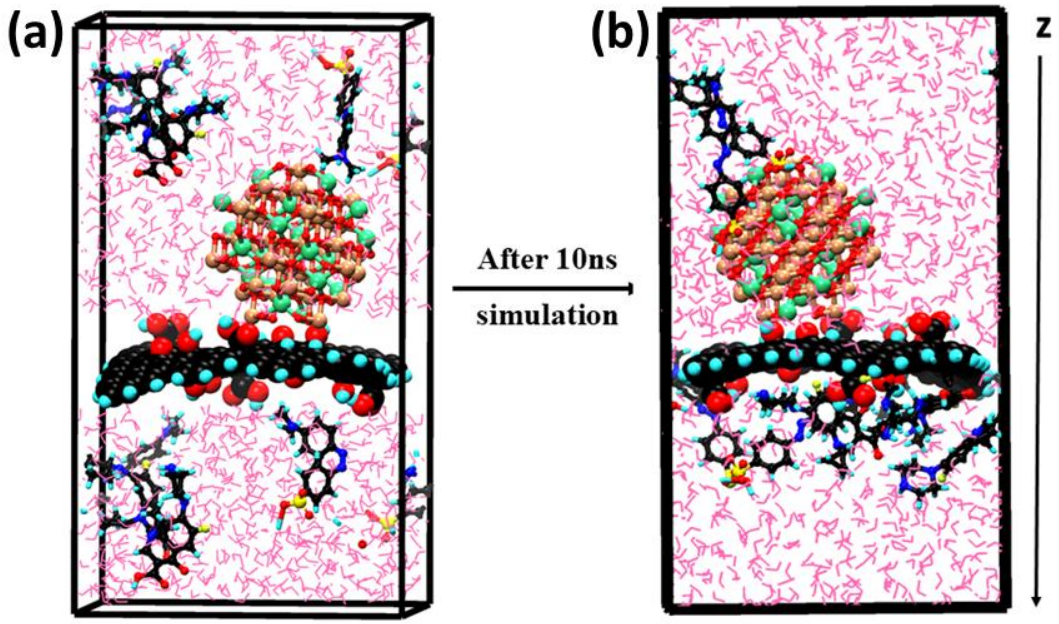

Figure 4.13 Snapshots of parallelopiped simulation box containing $NiFe_2O_4$ cluster and GO sheet surrounded by 4 CIP, 4 MG, and 1000 water molecules (a) at the start and (b) at the end of the simulation.

Figures 4.13a and 4.13b show the initial and the final system snapshots at the end of the ten-nanosecond MD run. As mentioned earlier, two MG and two CIP molecules were initially placed on either side of the GO sheet. The last configuration of the MD run shows that all CIP molecules have moved to the side of the GO sheet that does not have the $NiFe_2O_4$ cluster. Moreover, two MG molecules interact with particular atom types on the $NiFe_2O_4$ cluster through their sulphonic acid functionalities.

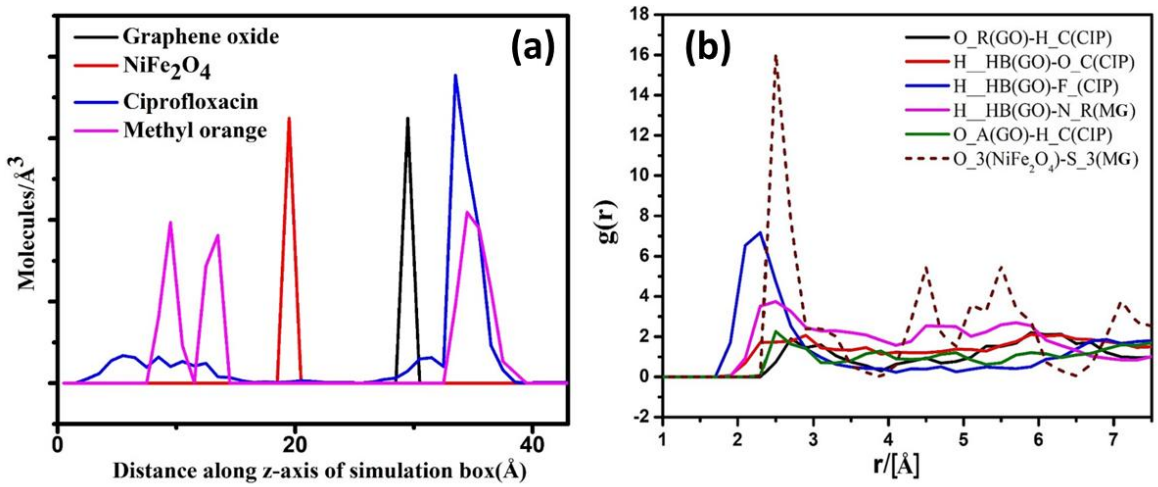

Figure 4.14 (a)Time-averaged density profile of CIP and MG molecules adsorbed over MNFGO, and (b) RDF graphs show interactions between different atom types of adsorbent and the adsorbate molecules. (Abbreviations: O_R - alcohol oxygen of GO; H_C- carboxylic H of CIP; H__HB - carboxylic H atom of GO; O_C- carbonyl oxygen of CIP; F_- fluoride group of CIP; N_R - azo N atom of MG dye; O_A - carboxylic O atom of GO; O_3 - lattice O of $NiFe_2O_4$; S_3 - sulfonic S atom of MG.)

Figure 4.14 (a) shows the time-averaged density profile for the last two ns of the MD run. The graph is plotted between molecules (of a type) per $Å^3$ versus distance along the z-axis of the simulation box. This time-averaged density profile confirms the inferences drawn from the snapshot at the end of the MD run. The MG (pink) peaks are adjacent to the $NiFe_2O_4$ cluster (red peak) and on one side of the GO sheet (black curve). But the blue (CIP) peaks are all on the side of the GO sheet with no $NiFe_2O_4$, indicating that CIP

interacts strongly with the GO oxygen functionalities. CIP molecules hardly interact with the $NiFe_2O_4$ cluster. At the same time, the MG molecules adsorb both by interaction with the $NiFe_2O_4$ cluster and the oxygen functional groups on the GO sheet.

The RDF or g(r) plots give the long-time average distances between different atom types comprising the system. The first peak of the RDF (Figure. 4.14(b)) between two atom types defines the typical interaction distance between them. The RDF analysis in this investigation is divided into three categories. These are interactions between atom types making MG and MNFGO, then CIP and MNFGO, CIP-MG[204,205]. The primary interactions among these are those between MG-MNFGO and CIP-MNFGO. Figure 4.14(b) shows the time-averaged RDF graph over the last 2 ns production run for MG-MNFGO and CIP-MNFGO interactions.

We first present the CIP-MNFGO RDF interactions (Figure. 4.14b). The blue curve represents the interaction between the carboxylic H atom of GO and the fluoride of CIP, while the red plot is for the interaction between the carboxylic H atom of GO and the carbonyl O atom of CIP interaction. The first peaks of the blue and the red plot appear at 2.2 and 2.3 Å respectively. The green plot represents the interaction between the carboxylic oxygen atom of GO and the carboxylic H of CIP. Its first peak appears at 2.4 Å. There is another interaction (black plot) between the alcohol oxygen of GO and carboxylic H of CIP. Its first peak is at 2.6 Å. Among all the CIP-MNFGO RDF plots, the first peak of the blue curve has the highest intensity, while the peak of the red curve has the next highest intensity. Hence, CIP interacts mainly with the GO part of MNFGO. Furthermore, the CIP-MNFGO interactions are dominated by those between the carboxylic H atom of GO and the fluoride of CIP and between the carboxylic H atom of GO and the carboxylic O atom of CIP interaction. Both are H-bond-type interactions[160].

The MG-MNFGO interaction RDF results are now presented. The first peak of the RDF (pink) plot between the carboxylic H atom of GO and the azo N atom of MG appears at 2.3 Å. Furthermore, the first peak of the (wine-colored) RDF plot between lattice O of $NiFe_2O_4$ and the sulfur of MG appears at 2.5 Å due to an electrostatic interaction[161]. The first peak of the wine-colored plot has a higher intensity than the other MG-MNFGO RDF interaction plot. Overall, an MG can approach the $NiFe_2O_4$ surface through an interaction via its sulfur atom and also by the interaction of its azo N-atom with the carboxylic H atom of GO. But the former interaction is much stronger than the latter.

It can be concluded that the CIP molecule adsorbs over the GO surface, while MG can adsorb through both $NiFe_2O_4$ and GO parts of MNFGO. Note that the strongest CIP interaction is between its F atom and the carboxylic H atom of GO. In contrast the MG adsorbs predominantly through the interaction between its sulphur and the lattice oxygen of the $NiFe_2O_4$ cluster. Thus, the adsorption sites for CIP and MG on the $NiFe_2O_4$/GO composite are separate facilitating co-adsorption.

4.4 Conclusions

A magnetically recyclable $NiFe_2O_4$/GO composite was investigated for the competitive adsorption of CIP and MG from their aqueous solutions. The composite was prepared by a hydrothermal method. Ni^{2+} and Fe^{3+} in the $NiFe_2O_4$/GO composite occupy octahedral and tetrahedral sites of the anion sublattice. Such occupancy is contrary to that observed in only $NiFe_2O_4$. CIP adsorption capacity was higher than MG's in the competitive adsorption scenario. The adsorbent demonstrated excellent recyclability for four cycles. The EF isotherm best fits the q_{ei} versus C_{ei} plots for CIP and MG. An EF isotherm fit indicates an adsorbent with heterogeneous adsorption sites, in conformity with the fact that $NiFe_2O_4$/GO adsorbent is a composite with different types of adsorbent sites. The nature of the diverse adsorption sites on the $NiFe_2O_4$/GO adsorbent utilized by CIP and MG adsorbates were

investigated by classical MD investigations. The MD simulation results showed that CIP interacts with the GO part of the composite through its alcohol and –COOH functional groups. MG adsorbs via its sulfonic acid group and azo nitrogens. The sulfonic acid part interacts with the $NiFe_2O_4$ lattice oxygen, while the azo nitrogen shows an H-bond type interaction with the –COOH group of the GO part of the composite. Such molecular-level adsorption mechanism insights are valuable for designing improved adsorbents.